Highly Efficient Coaxial TiO2-PtPd Tubular Nanomachines for Photocatalytic Water Purification with Multiple Locomotion Strategies

Journal Article

Author(s):
Musthaq, Fajer; Asani, Agim; Hoop, Marcus; Chen, Xiang-Zhong; Ahmed, Daniel; Nelson, Bradley J.; Pané, Salvador

Publication date:
2016-10

Permanent link:
https://doi.org/10.3929/ethz-b-000118858

Originally published in:
Advanced Functional Materials 26(38), https://doi.org/10.1002/adfm.201602315

Article type: Full Paper

Highly Efficient Coaxial TiO_2-PtPd Tubular Nanomachines for Photocatalytic Water Purification with Multiple Locomotion Strategies

By *Fajer Mushtaq, Agim Asani, Marcus Hoop, Xiang-Zhong Chen,* Daniel Ahmed, Bradley J. Nelson, and Salvador Pané**

F. Mushtaq, A. Asani, M. Hoop, Dr. X.-Z. Chen, Dr. D. Ahmed, Prof. Dr. B. J. Nelson, Dr. S. Pané

Multi-Scale Robotics Lab (MSRL), Institute of Robotics and Intelligent Systems (IRIS), ETH Zurich, CH-8092 Zurich, Switzerland.

E-mail: chenxian@ethz.ch, vidalp@ethz.ch

Keywords: TiO_2; Visible light photocatalysis; Core-shell nanotubes; Electrochemical synthesis; Micromanipulation

Abstract

Titania is a promising photocatalyst for water purification or production of solar fuels. However, due to its large bandgap, titania is photoactive solely under UV light, which accounts for less than 5% of the solar spectrum. In this work, we have designed and fabricated TiO_2-based hybrid one-dimensional nanostructures with photocatalytic activities extended to visible light region. Highly efficient coaxial TiO_2-PtPd-Ni nanotubes were fabricated by a template-assisted electrochemical synthesis route for water remediation under UV light, visible light and natural sunlight. These coaxial hybrid nanotubes displayed a 100% degradation of organic pollutant rhodamine B in only 50 min (*k*-value 0.071 min^{-1}) and 30 min under visible light and natural sunlight, respectively. For comparison, TiO_2 nanotubes doped with Pd nanoparticles were also fabricated and they showed inferior photocatalytic properties and degrading stability over time. The multicomponent design enabled us to actuate the hybrid NTs by using two different external energy sources i.e. magnetic and acoustic fields. Self-propelled, autonomous actuation in the presence of H_2O_2 was also realized. These versatile actuation modes have the potential to enable the reported photocatalytic nanomachines to work efficiently under complex environments and to be easily collected for re-use.

1. Introduction

Environmental pollution caused by increasing industrialization is one of the major problems imposed on modern society.[1] It is suggested that more than 14,000 deaths are reported daily due to waterborne diseases.[2] Industry is the biggest polluter of water bodies, with the textile industry discharging more than 200,000 tons of toxic synthetic dyes every year into effluents due to inefficiencies in the dyeing process.[3] The presence of even trace amounts of such synthetic dyes in water is considered harmful due to their high chemical oxygen demand (COD) and carcinogenic nature.[2a, 4] Pollutants are also responsible for negatively altering aquatic ecosystems by blocking the penetration of sunlight and oxygen, essential for the survival of various aquatic forms.[5] Unfortunately, due to their high stability, most of these recalcitrant dyes escape conventional wastewater treatment processes such as pre-chlorination, flocculation, coagulation and flotation and persist in the environment.[1, 6] Consequently, there is an ever-increasing need to develop efficient, cost-effective and green techniques for water purification. The heterogeneous advanced oxidation process (AOP) is one of the most extensively studied approaches, where toxic organic dyes are completely degraded into harmless by-products such as CO_2 and H_2O. AOPs are based on the in-situ generation of highly reactive species, such as hydroxyl and superoxide anion radicals ($OH^{\bullet}$ and $O_2^{\bullet-}$, respectively), by semiconductor photocatalysts for degradation of organic compounds.[7]

Due to its large band-gap, nontoxicity, low cost and abundant availability, titanium dioxide (TiO_2) is one of the most extensively studied semiconductors for photocatalysis.[8] A wide band-gap provides sufficient charge separation between the photogenerated electron-hole pairs, hence retarding their recombination and increasing the efficiency of the system.[9] However, this wide band-gap also limits the use of TiO_2 to only UV light, which accounts for less than 5% of the solar spectrum.[10] To extend TiO_2's optical response into visible light, many attempts have been explored to modify its band gap. These measures include doping and coupling TiO_2 with nonmetals (e.g. sulfur, carbon, nitrogen), semiconductors, and

metals.[11] Among these techniques, fabrication of heterostructures of TiO_2 with noble metals such as gold (Au), silver (Ag), platinum (Pt) or palladium (Pd) has proven to be one of the most efficient approaches.[12] The combination of an n-type semiconductor like TiO_2 with a noble metal creates a Schottky barrier at their interface. This Schottky barrier is responsible for enhancing electron-hole charge separation and hence, is responsible for prolonging the lifetime of these charge carriers.[13] Moreover, when TiO_2 is coupled with bimetallic noble metals such as platinum-copper, silver-palladium or platinum-palladium, its photocatalytic activity is much higher.[14] For example, TiO_2 loaded with bimetallic platinum-palladium nanoparticles (NPs) exhibited a photocatalytic activity that was 19 times higher than that of pure TiO_2 and about approximately four times higher compared to coupling only monometallic Pd NPs to TiO_2.[14a]

Besides appropriate material selection, development of highly efficient photocatalysts also requires selection of their optimal size and architecture. Due to the very high specific surface area of one-dimensional nanowires (NWs) and nanotubes (NTs), they are ideal candidates to develop solar cells and photocatalysts for water remediation and water splitting.[15] With a charge carrier diffusion length of about 20 nm, TiO_2 nanostructures with a thickness of less than 20 nm are optimal for providing efficient charge separation. [13a, 16] This makes thin TiO_2 NTs with a high aspect ratio an attractive choice to fabricate efficient photocatalysts. Two major approaches are commonly used to combine noble metals with TiO_2, which includes either depositing NPs on the surface of TiO_2 or fabricating core-shell noble metal-TiO_2 nanospheres.[17] Photocatalysts based on NPs deposited on a TiO_2 surface have shown a reduced stability caused by dissolution or photocorrosion of NPs in their surrounding environment.[12a, 18] In contrast, the architecture exhibited by encapsulation of noble metals around a TiO_2 shell could lead to development of more efficient and durable photoactive materials in the future.[18-19] Presently, various synthesis routes are available for fabrication of high specific surface area TiO_2 nanostructures.[8a, 11c] Unfortunately, these techniques lack

control over the growth parameters and suffer from the inability to fabricate multicomponent nanostructures. However, electrochemical synthesis can be used to fabricate hybrid TiO_2 nanostructures with a high degree of control over their morphology, composition, and design.[20]

Another important fact that prevents photocatalysts from being used for practical water purification applications is a lack of control over their motion and swimming characteristics.[21] Most current micro- and nanostructures are designed to be propelled using a single power source such as external magnetic fields, electric fields, light, or by decomposition of chemical fuels such as hydrogen peroxide.[22] This restriction causes secondary pollution due to their loss and renders them costly and ineffective under harsh, changing environments. Hence, there is a growing need to fabricate hybrid micro-/nanomachines that are capable of achieving efficient propulsion by using multiple power sources.[23] Achieving such a multimode propulsion strategy requires careful design and efficient implementation of a multicomponent nanovehicle within a single nanoscale entity.

In this work, we present nanomachines composed of coaxial TiO_2-noble metal (Pt, PtPd) NTs filled with nickel nanowires for photocatalytic water remediation under UV, visible light, and natural sunlight. An electrochemical synthesis route was chosen to fabricate these multicomponent nanostructures by sequential template-assisted electrodeposition. This approach provided a unique fabrication platform to study the enhancement in photocatalytic activity offered by noble metals coupled to TiO_2 NTs as NPs and NTs. Comparison in the photocatalytic efficiency offered by bimetallic PtPd NTs versus monometallic Pd NTs was also investigated. Additionally, these hybrid NTs demonstrated versatile actuation modes such as fuel-powered autonomous actuation as well as fuel-free magnetic and acoustic field guided swimming behavior.

2. Results and discussion

TiO_2 nanotubes were deposited inside commercially available anodized aluminium oxide (AAO) templates by an electrochemically induced sol-gel technique (**Figure 1**a (i, ii)). When a potential greater than - 0.9 V *vs.* Ag/AgCl was applied, nitrate present in the solution was reduced to form hydroxyl ions causing a local increase in pH near the electrode.[24] The pH increase induced formation of titanium hydroxide gel within the AAO pores.[16, 24] This gel was then thermally treated using two approaches in which AAO templates were either dried overnight at 100 ˚C ($T_{\_100}$) to remove water or directly annealed at 650 ˚C for 2 h ($T_{\_650}$) to form crystalline TiO_2 NTs. TiO_2 NTs dried at 100 ˚C were filled with Pd by electrodeposition (Figure 1a (iii)) and the NTs were eventually annealed at 650 ˚C in order to allow crystallization ($TP_{\_650}$). Apart from this, Pd and PtPd NTs were also electroplated inside the AAO templates that were previously filled with TiO_2 NTs annealed at 650 ˚C (Figure 1a (iv)) ($T_{\_650}P$, $T_{\_650}PP$). These hybrid NTs were filled with Ni nanowires to efficiently collect them using a magnet. This was followed by wet etching of the AAO template to release the NTs (Figure 1a (v-vi)). Figure 1b presents the scanning electron microscopy (SEM) image obtained from freestanding $TP_{\_650}$-Ni NTs, and the inset shows their magnified image. We can observe the presence of many randomly distributed NPs on the surface of TiO_2 NTs. Figure 1c presents the high angle annular dark (HAADF) scanning transmission electron microscopy (STEM) image of a single $TP_{\_650}$ NT, where we can see its uniform NW structure. From the corresponding energy-dispersive X-ray (EDX) mappings obtained, we can clearly observe the presence of a TiO_2 NT with randomly distributed Pd NPs encapsulating a Ni NW. The reason behind the formation of Pd NPs could be the inability of the titania gel to form dense shells due to the insufficient heat treatment, causing the Pd ions to penetrate the gel during electrodeposition.[16] As a result, Pd nuclei formed when such ions combined with an electron and during the subsequent annealing step at 650 ˚C, these Pd NPs diffused into the TiO_2 phase. Figure 1d shows the top-view of freestanding $T_{\_650}P$-Ni NT arrays and the inset shows their

magnified image. A STEM image obtained for this sample is presented in Figure 1e, where a uniform shell can be seen around a nanowire. From this image, we can clearly observe that this hybrid nanostructure has conformal interfaces between its different components. According to the EDX mappings obtained for the elements, this outer shell clearly corresponds to a 15 nm-thick TiO_2 layer, followed by a Pd NT and Ni NW. Superimposed EDX map for Ti, O and Pd elements further depicts a TiO_2 shell homogeneously encapsulating a Pd NT.

The crystalline structure of the hybrid NTs was analyzed using TEM and X-ray diffraction (XRD) (**Figure 2**a). XRD investigation performed on these NTs showed that all samples possessed a good crystallinity, apart from the amorphous $T_{\_100}$ sample (data not shown). XRD investigation of $T_{\_650}$ NT sample revealed that the TiO_2 phase structure consists of a mixture of anatase, rutile and brookite polymorphs. The presence of all three polymorphs has been previously shown to have a positive effect on the photocatalytic activity of TiO_2.[25] Analysis of the diffraction peaks at 25.4°, 38.3° and 75.3° can be observed corresponding to the (101), (112) and (224) faces of anatase TiO_2 (JCPDS file no. 73-1764). Similarly, 27.4°, 54.8° and 56.5° peaks can be ascribed to (110), (211) and (220) crystal planes of rutile TiO_2 (JCPDS file no. 73-1765) and reflections at 31.7°, 33.6°, 42.0°, 70.6° and 71.6° can be assigned to brookite TiO_2 (JCPDS file no. 16-0617). Analysis of $T_{_650}$P-Ni NTs showed new peaks at 40.1°, 46.7° and 68.2° assigned to the (111), (200) and (220) faces of cubic Pd (JCPDS file no. 46-1043) and reflections at 44.6°, 51.8°, 64.6° and 76.4° corresponding to the (111), (200), (012) and (220) crystal planes of cubic Ni (JCPDS file no. 04-0850), respectively. XRD analysis of $T_{_650}$PP-Ni NTs also revealed new peaks at 38.9°, 45.6° and 66.2° that can be ascribed to the (111), (200) and (220) faces of cubic Pt (JCPDS file no. 04-0802).

A TEM image showing the top-end of two over-lapping $T_{_650}$PP-Ni NTs is presented in Figure 2b. From this image, we can observe the presence of a thin shell, which encapsulates

a NT with a dark contrast. The inset, shows the selected area electron diffraction (SAED) pattern of these NTs, where the presence of multiple rings confirms that the structures are polycrystalline in nature. High-resolution transmission electron microscopy (HRTEM) analysis performed on the outermost shell is presented in Figure 2c. From this, we can observe a 15 nm-thick polycrystalline layer having multiple growth orientations. Further analysis shows the presence of d-values of 0.324 nm and 0.350 nm, corresponding to TiO_2 anatase (101) and rutile (110) planes. In contrast, by analyzing the HRTEM image obtained from the NT with a dark contrast (Figure 2d), presence of PtPd NT could be identified from the d-spacings of 0.196 nm and 0.224 nm (Pt (200) and Pd (111), respectively).

The photocatalytic performance of all NTs was evaluated by studying the degradation of a rhodamine-B (RhB) solution under UV, visible light, and natural sunlight for 1 h using continuous magnetic agitation. The degradation curves obtained under UV light show that all the samples exhibited a gradual degradation over time except the control that showed negligible response (**Figure 3**a). Due to their high crystallinity, all the samples that were annealed at a high temperature (650 ˚C) showed a better performance than the ones dried at 100 ˚C ($T_{\_100}$). The bimetallic $T_{_650}$PP NTs were the most efficient photocatalysts with a 93% dye degradation in 1 h. From Figure 3b, we can observe that the trend of dye degradation of NTs in the presence of visible light is similar to their response under UV light, where all the NTs displayed a gradual degradation of RhB over time and the bimetallic samples were the best performing photocatalyst.

A quantitative analysis of the degradation rates offered by the high temperature annealed samples is given by comparing their reaction rate constant *k*, which can be defined by,

$$k = \ln\left(\frac{C_0}{C}\right)/t \qquad (1)$$

where, C_o is the initial RhB concentration and C is the RhB concentration at time t. The calculation is based on the assumption that the kinetics of RhB degradation reaction catalyzed by these NTs are (pseudo-)first-order reactions. These results are presented in Figure 3c where we can observe that pure TiO_2 $T_{\_650}$ NTs showed a poorer performance under visible light than under UV light. Conversely, the hybrid NT samples coupled with noble metals (i.e. Pt or PtPd) performed better under visible light than under UV light. While hybrid NTs didn't show any significant improvement than the pure TiO_2 NTs under UV light, coupling TiO_2 nanotubes with Pd nanoparticles ($TP_{\_650}$), Pd nanotubes (T_{650}_P) and PdPt nanotubes (T_{650}_PP) gives 3.2, 5.8, and 9.6 times higher *k*-values than pure TiO_2 under visible light. The best performing photocatalysts were the $T_{_650}$PP NTs that demonstrated 100% degradation of RhB under visible light within 50 min. With a *k*-value of 0.071 min^{-1}, $T_{_650}$PP NTs are one of the most efficient visible light photocatalysts to have been reported (see Table S1).

To better explain this improved dye degradation performance of hybrid coaxial NTs under visible light, we first look into the underlying mechanism of photocatalysis of TiO_2. Upon light irradiation, electrons are excited from the valence band (VB) of TiO_2 to its conduction band (CB), leaving behind holes in its VB and, thus, creating electron-hole pairs on the surface of the semiconductor.[26] Electron-hole pairs are responsible for initiating photocatalytic reactions by converting oxygen and water to form highly reactive species such as $OH^{\bullet}$ and $O_2^{\bullet-}$. These radicals play a crucial role in the photocatalytic degradation of organic molecules like RhB into harmless products (Figure 3d) However, the band gap of TiO_2 ranges from 2.98 eV to 3.26 eV, depending on its crystalline phase, which limits its light absorption to only the UV region. As can be observed from the UV-Vis diffuse reflectance spectra (DRS) (Figure 3e), the $T_{\_650}$ NTs exhibited a light absorption only within the 250-380 nm range, which can justify their poor photocatalytic activity under visible light (band-gap of 3.02 eV). Coupling TiO_2 with nanosized noble metal structures extends its absorption band into the visible light region, as shown in Figure 3e. Based on the DRS measurement their band-gaps

can be calculated as 2.82 eV, 2.84 eV and 2.83 eV for $TP_{\_650,}$ $T_{\_650}P$ and $T_{\_650}PP$ NTs, respectively. Besides, these noble metal nano structures absorb visible light to generate collective oscillation of valence electrons known as the localized surface plasmon resonance (LSPR). The light excited electrons on the surface of noble metals must overcome the Schottky barrier (ϕ, difference between the CB of the semiconductor and the work function of metal) created at the interface of semiconductor/metal heterojunction in order to be transferred to the TiO_2 phase.[14b, 27] The CB of TiO_2, being an electron acceptor,[28] readily accepts the electrons from Pd or PtPd, hence promoting diffusion of electrons into the TiO_2 shell (Figure 3d). Thus, by coupling noble metals to TiO_2 NTs, electron-hole pairs can be efficiently generated under visible light. By comparing Figure 3c and Figure 3e, we can find that under visible light, the normalized absorbed intensity exhibits a positive correlation with the *k*-values. A higher photocatalytic efficiency is observed in NTs with a continuous interface ($T_{\_650}P$) than in samples with randomly distributed NPs ($TP_{\_650}$). Possible explanations for this phenomenon could be that in $TP_{\_650}$ NTs there is a larger availability of Pd catalyst and an increased interface area between TiO_2 and Pd. This can increase the absorption of light and, hence, generate more electron-hole pairs to participate in the photocatalytic degradation process. Another important result obtained shows that the bimetallic NTs ($T_{\_650}PP$) are 1.7 times more efficient than the monometallic NTs ($T_{\_650}P$). This result can be explained by the fact that combining Pd with Pt lowers its work function, and, therefore, reduces the height of the Schottky barrier.[14a, 29] A lowered Schottky barrier is able to promote electron transfer from the PtPd NTs to the TiO_2 phase much more efficiently,[14b, 30] hence making the bimetallic $T_{\_650}PP$ NTs better photocatalysts.

The improvement in photocatalytic activity under UV light is not as prominent as under visible light. This slightly increased efficiency in $T_{\_650}P$ and $T_{\_650}PP$ NTs may arise from the fact that noble metals act as electron traps and decrease the electron-hole recombination rate.[9b, 18] A closer look at the graph shows that under UV light, $TP_{\_650}$ NTs

exhibited a slower degradation rate than $T_{\_650}$ NTs. This trend can be attributed to the presence of many randomly distributed Pd NPs all over the TiO_2 matrix. Such a random NP distribution all over the TiO_2 surface can reduce the total photoactive area of TiO_2 NTs and, hence, reduce their photoactivity.[16, 31]

To develop practical photocatalysts for water purification, it is important that they are not only efficient but also highly stable so that they can be reused. The reusability of coaxial $T_{_650}$P NTs and NP coupled $TP_{\_650}$ NTs are examined and presented in Figure 3f. In the case of coaxial $T_{_650}$P NTs, all three runs had almost similar and stable degradation rates, expressed by their *k*-values, 0.0425 min^{-1}, 0.0425 min^{-1} and 0.0418 min^{-1}, respectively. $TP_{\_650}$ NTs exhibited a gradually decreased photocatalytic activity with each consecutive run (0.0244 min^{-1}, 0.0226 min^{-1}, and 0.0174 min^{-1}), respectively. This unstable reusability trend shown by the $TP_{\_650}$ NTs can be caused by the photocorrosion or dissolution of Pd NPs in their surrounding environment over time.[17a, 17b] Our results suggest that noble metals should be shielded from the surrounding media by designing core-shell structures instead of using them as NPs, as has been indicated elsewhere.[12a, 18]

Photocatalytic efficiencies of our NTs was also studied under natural sunlight to demonstrate that they can be used for practical water purification applications at a similar [Dye]/[$T_{_650}$PP] weight ratio of 0.006 (Figure 3g). We can observe almost similar degradation trends as obtained under a visible light lamp. This study shows that our coaxial NTs, especially $T_{_650}$PP NTs that degraded 100% of the dye in just 30 min, can serve as efficient photocatalysts to destroy organic pollutants under sunlight. To further demonstrate the practical use of $T_{_650}$PP NTs under direct sunlight, we also investigated the photocatalytic degradation of three different organic dyes i.e. RhB, methyl orange (MO) and methylene blue (MB) at much elevated concentrations of 12 mg L^{-1} ([Dye]/[$T_{_650}$PP] = 0.018). Figure 3h presents a collage of images taken every 20 minutes to represent how the $T_{_650}$PP NTs were successful in degrading all three dyes in less than 2 h, even at much higher dye concentrations.

This result further highlights the versatile and efficient nature of water remediation offered by our hybrid nanotubes.

To ensure that these hybrid NTs can be guided to specific locations and efficiently collected for re-use, $T_{_650}$PP-Ni NTs were tested to study their response in the presence of external fields and/or fuels such as H_2O_2 solution. The novel architecture of these coaxial NTs coupled with Ni nanowires, enabled their use under three different propulsion mechanisms, i.e. under wireless magnetic and acoustic fields and as self-propelled catalytic nanomachines (**Figure 4**a-d). Rotational magnetic fields were applied to a single $T_{_650}$PP-Ni NT released in deionized (DI) water. It was possible to precisely guide the hybrid NT along a pre-planned trajectory, as can be seen from the time lapse image in Figure 4a and Video S1. A single, self-propelled $T_{_650}$PP-Ni NT demonstrated autonomous actuation in the presence of 5% H_2O_2 solution. Here, the PtPd NT decomposed the H_2O_2 solution into water and oxygen bubbles, giving rise to a self-propelled motion, powered by ejection of oxygen bubbles from the PtPd NT (Figure 4b and Video S2). Figure 4c and Video S3, illustrates dual motion exhibited by a single $T_{_650}$PP-Ni NT in H_2O_2 solution and under wireless magnetic fields. From this time-lapse image, it can be clearly seen that static magnetic fields can be used to precisely guide the direction of movement of these autonomous nanomachines. $T_{_650}$PP-Ni NTs can also be powered wirelessly using acoustic fields as shown in Figure 4d and Video S4, where a single NT displayed an efficient linear propulsion. Hence, by optimal material selection and careful design of our nanomachines, three different locomotion techniques were demonstrated by hybrid $T_{_650}$PP-Ni NTs. Such versatile actuation exhibited by a single nanomachine can offer a diverse and flexible scope of operation, depending upon its mission or upon changes in its surrounding environment.[23a] The importance of developing smart photocatalysts that can be easily actuated is further highlighted by comparing the degradation curves obtained under static versus continuous agitation plots presented in **Figure S4**a and b. From these plots one can see that, without any magnetic actuation our nanotubes displayed much lower

photocatalytic activity. This could be due to their sedimentation in the absence of any actuation and hence, reduced active surface area availability for the degradation process.

In order to use these hybrid NTs to clean water sources with aquatic life, it is important to ensure that they are biocompatible. Therefore, the interaction between the $T_{_650}$PP-Ni NTs and NIH 3T3 cells was examined for 48 h. Figure 4e shows an optical image of healthy fibroblast cells interacting with the hybrid NTs. To further demonstrate this, we also performed nucleus and actin filament staining which showed viable cells growing over the hybrid NTs (Figure 4f). Additionally, MTT assay was also performed to test the biocompatibility of our hybrid $T_{_650}$PP-Ni NTs after 48 h, and they showed a cell viability of 80% even when NT concentration was as high as 75 ppm (0.075 mg mL^{-1}) (Figure S5). These results demonstrate that our hybrid NTs are non-cytotoxic.

3. Conclusions

In conclusion, we have developed an architecture to create highly efficient visible light photocatalysts for water remediation. These photocatalysts are composed of TiO_2 NTs and noble metals present either as NPs or as coaxial NTs using an electrochemical fabrication approach. We were able to compare for the first time the efficiency of TiO_2 NTs coupled to noble metals as NPs and as NTs. TiO_2-Pd monometallic NTs, TiO_2-PtPd bimetallic NTs and TiO_2 NTs decorated with Pd NPs were fabricated. We observed that coaxial TiO_2-Pd NTs exhibited a much higher efficiency and stability in comparison to TiO_2 NTs covered with Pd NPs. Furthermore, when TiO_2 NTs coupled with bimetallic PtPd NTs were used, they demonstrated a much faster degradation rate in comparison to TiO_2 NTs coupled with monometallic Pd NTs. The most efficient photocatalysts, with a *k*-value of 0.071 min^{-1}, were the TiO_2-PtPd coaxial NTs, which were able to degrade the organic pollutant RhB, in situ, with a 100% efficiency in 50 min and 30 min under visible light and natural sunlight, respectively. The unique design of hybrid TiO_2-PtPd-Ni NTs, apart from their enhanced

photocatalytic performance, also provided the advantage of optimally harvesting both fuel-free and fuel-powered actuations. Such versatile propulsion mechanisms make these hybrid nanomachines cost-effective and highly efficient photocatalysts that can be precisely controlled and collected for re-use. Biocompatibility demonstrated by these nanomachines further confirms their possible utilization for water purification with aquatic life. The hybrid nanomachines developed in this work are attractive candidates for designing future water remediation and water splitting photocatalysts and display efficient motion under complex, challenging environments.

4. Experimental section

Fabrication of TiO_2 nanotubes: Commercially available AAO templates with a pore diameter of 200 nm were purchased from *Whatman Anodisc*. 100 nm Au was evaporated by electron beam evaporation on one side of the template that served as a conductive working electrode. Prior to deposition, the Au covered side of the template was isolated to ensure exclusive deposition inside the pores. Electrodeposition was carried out using an Autolab PGSTAT302N, in a three-electrode setup with Pt sheet as a counter electrode and a Ag/AgCl (3 M KCl) reference electrode. TiO_2 nanotubes were fabricated at room temperature from an electrolyte solution consisting of 0.02 M titanium oxysulfate ($TiOSO_4$), 0.03 M hydrogen peroxide (H_2O_2), 0.05 M HNO_3 and 0.25 M KNO_3 at a pH of 1.4.[16, 24] Deposition was carried out potentiostatically at a constant voltage of -1.00 V for 6 h. After deposition, the AAO templates were either dried overnight at 100˚C or annealed for 2 h at 650˚C in a tube furnace.

Fabrication of Pd, Pt-Pd nanotubes: For Pd and Pt-Pd NT fabrication, a three-electrode set-up was used with the AAO template filled with TiO_2 nanotubes serving as the working electrode, a Pt sheet acting as the counter electrode and a Ag/AgCl (3 M KCl) reference electrode. Pd electrodepostion was carried out potentiostatically at room temperature under

constant magnetic stirring at a potential of -0.1 V for 30 min inside $T_{\_650}$ NTs and for 10 min inside $T_{\_100}$ NTs. Plating solution consisted of 0.05 M $PdCl_2$ and 0.1 M HCl.[32] Pt-Pd bimetallic nanotubes were fabricated using the same setup as above at a potential of -0.1 V for 3 h with a plating solution consisting of 0.005 M $PdCl_2$, 0.005 M H_2PtCl_6 and 0.04 M HCl.[33]

Fabrication of Ni nanowires: For Ni nanowire fabrication, a similar three-electrode set-up was used with the AAO template filled with TiO_2 and Pd or Pt-Pd nanotubes serving as the working electrode, a Pt sheet acting as the counter electrode and a Ag/AgCl (0.1 M Na_2SO_4) reference electrode. Nickel electrodepostion was carried out potentiostatically at room temperature under constant magnetic stirring at a potential of -1.0 V for 2 min, using a plating solution consisting of 0.4 M $NiSO_4$ and 0.7 M boric acid. After deposition, the nanotubes were released by dissolving the AAO template in an aqueous solution of 5 M NaOH for 2 h followed by washing them with DI water five times using ultrasonification. Finally, the nanotubes were collected using centrifugation and stored in DI water.

Material characterization: Morphology of the resulting nanotubes was studied by scanning electron microscopy (SEM, Zeiss ULTRA 55, Zeiss, Oberkochen, Germany), transmission electron microscopy (TEM, FEI F30, FEI Co., Hillsboro, OR), and scanning transmission electron microscopy (STEM, FEI F30). The composition and crystallographic structure of the nanotubes were analyzed by energy-dispersive X-ray analysis (EDX) and X-ray diffraction (XRD, Bruker AXS D8 Advance). Distribution of elements along the nanotubes was studied by EDX mapping using HAADF STEM (FEI Talos F200X). Local crystallographic structure was studied by selected area electron diffraction (SAED). UV-Vis diffuse reflectance spectra (DRS) was acquired by a Cary 4000 UV-vis spectrophotometer. $BaSO_4$ was used as the reflectance standard and the ratio of our sample to $BaSO_4$ was kept constant with respect to the quantity of TiO_2.

Photocatalytic characterization: Photocatalytic experiments were performed at ambient temperature and pressure to study the degradation of RhB dye in the presence of our nanotube structures after the adsorption-desorption equilibrium was reached. An RhB concentration of 4 mg L^{-1} was chosen to perform degradation experiments under continuous magnetic agitation. 10 mg of released pure TiO_2 and 20 mg of hybrid nanotubes (one whole electroplated AAO template in each case) were dispersed in 30 mL of RhB solution and were magnetically stirred. The samples were irradiated with UV-visible light using a 450 W Xenon lamp (Oriel, model 66929: 450 W), where the distance between the lamp and the samples was fixed to 15 cm. Visible light illumination ($\lambda > 420$ nm) was provided by a colored glass filter (Newport) and UV light illumination was obtained by using a filter with $\lambda < 400$ nm (Edmund Optics). A UV-Vis spectrophotometer (Tecan Infinite 200 Pro) was used to obtain the fluorescent spectra of RhB over time by taking aliquots of irradiated RhB solution every 10 minutes (50 µL) for 1 h.

Manipulation experiments: Hybrid $T_{_650}$PP-Ni nanotube structures were used for manipulation experiments. The magnetic manipulation system consists of eight stationary electromagnets with soft magnetic cores, capable of producing magnetic fields and gradients up to 50 mT and 0.5 T m^{-1} at frequencies up to 100 Hz. The system is integrated with an inverted fluorescence microscope (Olympus IX 81) and videos of manipulated structures were recorded under rotational and static magnetic fields at 40x magnification (Videos S1 and S3). Manipulation experiments in H_2O_2 were performed by adding 5% H_2O_2 solution to the $T_{_650}$PP-Ni NTs and videos of NTs were recorded at 40x (Videos S2 and S3). Manipulation of hybrid $T_{_650}$PP-Ni NTs was perfomed by studying their propulsion in a complex standing wave field. A standing wave field was formed by introducing acoustic waves via a piezoelectric transducer bonded on a glass slide adjacent to the liquid droplet. The droplet was

then sandwiched between glass slides. Acoustic fields at a frequency of 366 kHz and output amplitude of 10 Vp-p were used to propel $T_{\_650}PP$ nanotubes (Video S4, 40x magnification).

Biocompatibility test: NIH 3T3 cells (American Type Cell Culture, ATCC) were expanded in high glucose (4.5 g L^{-1}) DMEM containing (GIBCO), 10% fetal calf serum and 100 units mL^{-1} Penicillin and 100 mg mL^{-1} Streptomycin. The cells were labeled with Hoechst 33342 (Sigma) and Alexa 488 Phalloidin (Sigma). Phase-contrast and fluorescence images were taken with an IX 81 Olympus camera at 20x magnification. The MTT Cytotoxicity study was conducted in a flat bottomed 96-well tissue culture plate with 4×10^3 3T3 cells in 100 µL culture medium (DMEM, 10% FCS, 1× Antimycoticum) per well. Cells were allowed to attach on the surface for 5 hours. Then the cell culture medium was supplemented with the hybrid nanotubes at different concentrations (0-75 ppm). After 48 h of incubation at 37 °C and 5 % CO_2, 10 µL of 12 mM MTT were added. Cells were further incubated for 4 h for MTT cleavage at 37 °C. Then, 100 µL of isopropanol and 0.04 M HCl were added to each well and mixed thoroughly until the formazan crystals were dissolved. Absorbance measurements were conducted in a micro-titer plate reader (Infinite F200 Tecan) at 570 nm. Reported values are represented as mean values of five independent replicates as percentages with respect to the control sample (Figure S5).

Supporting Information

Acknowledgements

This work has been financed by the European Research Council Starting Grant "Magnetoelectric Chemonanorobotics for Chemical and Biomedical Applications (ELECTROCHEMBOTS)", by the ERC grant agreement no. 336456. The authors would like

to acknowledge the Scientic Center for Optical and Electron Microscopy (ScopeM) of ETH Zurich, the Institute of Geochemistry and Petrology and the FIRST laboratory, ETH Zurich for their technical support. The authors would also like to thank Kakeru Fujiwara from ETH Zurich for providing the UV-Vis lamp set-up, Dr. Alla Sologubenko from ETH Zurich for help with EDX mappings. The authors would like to acknowldge Dr. Davide Ferri from the Paul Scherrer Institute (PSI) for help with DRS measurements and Dr. Eva Pellicer from Universitat Autònoma de Barcelona for all her support.

Received: ((will be filled in by the editorial staff))
Revised: ((will be filled in by the editorial staff))
Published online: ((will be filled in by the editorial staff))

[1] A. Matilainen, M. Vepsäläinen, M. Sillanpää, *Adv. Colloid Interface Sci.* 2010, **159**, 189.

[2] a) R. Kant, *J. Nat. Sci.* 2012, **4**, 22; b) M. A. Fox, M. T. Dulay, *Chem. Rev.* 1993, **93**, 341.

[3] a) B. Padhi, *Int. J. Env. Sci.* 2012, **3**, 940; b) F. Chequer, G. Oliveira, J. C. E. Ferraz, M. Zanoni and D. Oliveira, *Eco Friendly Textile Dyeing and Finishing*, InTech, 2013.

[4] P. V. Kamat, D. Meisel, *C. R. Chim.* 2003, **6**, 999.

[5] E. M. Saggioro, A. S. Oliveira, T. Pavesi, C. G. Maia, L. F. V. Ferreira, J. C. Moreira, *Molecules* 2011, **16**, 10370.

[6] D. Mohan, C. U. Pittman Jr, *J. Hazard Mater.* 2007, **142**, 1.

[7] a) S. Malato, P. Fernández-Ibáñez, M. I. Maldonado, J. Blanco, W. Gernjak, *Catal. Today* 2009, **147**, 1; b) U. I. Gaya, A. H. Abdullah, *J. Photochem. and Photobiol. C: Photochem. Rev.* 2008, **9**, 1.

[8] a) H. S. M. Tabaei, M. Kazemeini, M. Fattahi, *Scientia Iranica* 2012, **19**, 1626; b) R. Singh, R. Bapat, L. Qin, H. Feng, V. Polshettiwar, *ACS Catal.* 2016, **6**, 2770.

[9] a) J. Tian, Y. Sang, G. Yu, H. Jiang, X. Mu, H. Liu, *Adv. Mater.* 2013, **25**, 5074; b) S. Sakthivel, M. V. Shankar, M. Palanichamy, B. Arabindoo, D. W. Bahnemann, V. Murugesan, *Water Res.* 2004, **38**, 3001.

[10] R. Ren, Z. Wen, S. Cui, Y. Hou, X. Guo, J. Chen, *Sci. Rep.* 2015, **5**, 10714.

[11] a) H. Zeng, J. Xie, H. Xie, B.-L. Su, M. Wang, H. Ping, W. Wang, H. Wang, Z. Fu, *J. Mater. Chem. A* 2015, **3**, 19588; b) J. Senthilnathan, L. Philip, *J. Chem. Eng.* 2010, **161**, 83; c) Y. Yang, P. Wang, *Polymer* 2006, **47**, 2683; d) M. Wang, L. Sun, Z. Lin, J. Cai, K. Xie, C. Lin, *Energy Environ. Sci.* 2013, **6**, 1211.

[12] a) N. Zhang, S. Liu, X. Fu, Y.-J. Xu, *J. Phys. Chem. C* 2011, **115**, 9136; b) I. Paramasivam, J. M. Macak, P. Schmuki, *Electrochem. commun.* 2008, **10**, 71.

[13] a) R. van de Krol, Y. Liang, J. Schoonman, *J. Mater. Chem.* 2008, **18**, 2311; b) J. Ma, M. Yang, Y. Sun, C. Li, Q. Li, F. Gao, F. Yu, J. Chen, *Physica E: Low Dimens. Syst. Nanostruct.* 2014, **58**, 24.

[14] a) A. Zielińska-Jurek, J. Hupka, *Catal. Today* 2014, **230**, 181; b) Y. Shiraishi, H. Sakamoto, Y. Sugano, S. Ichikawa, T. Hirai, *ACS Nano* 2013, **7**, 9287; c) J. He, I. Ichinose, T. Kunitake, A. Nakao, Y. Shiraishi, N. Toshima, *J. Am. Chem. Soc.* 2003, **125**, 11034.

[15] a) W. J. Youngblood, S.-H. A. Lee, K. Maeda, T. E. Mallouk, *Acc. Chem. Res.* 2009, **42**, 1966; b) C. Liu, J. Tang, H. M. Chen, B. Liu, P. Yang, *Nano Lett.* 2013, **13**, 2989.

[16] A. W. Maijenburg, J. Veerbeek, R. de Putter, S. A. Veldhuis, M. G. C. Zoontjes, G. Mul, J. M. Montero-Moreno, K. Nielsch, H. Schafer, M. Steinhart, J. E. ten Elshof, *J. Mater. Chem. A* 2014, **2**, 2648.

[17] a) X.-F. Wu, H.-Y. Song, J.-M. Yoon, Y.-T. Yu, Y.-F. Chen, *Langmuir* 2009, **25**, 6438; b) X.-F. Wu, Y.-F. Chen, J.-M. Yoon, Y.-T. Yu, *Mater. Lett.* 2010, **64**, 2208; c) C. Fang, H. Jia, S. Chang, Q. Ruan, P. Wang, T. Chen, J. Wang, *Energy Environ. Sci.* 2014, **7**, 3431.

[18] X. Zhang, S. Ye, X. Zhang, L. Wu, *J. Mater. Chem. C* 2015, **3**, 2282.

[19] Q. Dong, H. Yu, Z. Jiao, G. Lu, Y. Bi, *RSC Adv.* 2014, **4**, 59114.

[20] a) T. Y. Seiichi Sawatani, Tomokazu Ohya, Takayuki Ban, Yasutaka Takahashi and Hideki Minoura, *Electrochem. Solid State Lett.* 2005, **8**, C69; b) C. N. a. G. Nogami, *J. Electrochem. Soc.* 1996, **143**, 1547.

[21] F. Mushtaq, M. Guerrero, M. S. Sakar, M. Hoop, A. M. Lindo, J. Sort, X. Chen, B. J. Nelson, E. Pellicer, S. Pane, *J. Mater. Chem. A* 2015, **3**, 23670.

[22] a) W. Gao, S. Sattayasamitsathit, J. Orozco, J. Wang, *J. Am. Chem. Soc.* 2011, **133**, 11862; b) X.-Z. Chen, N. Shamsudhin, M. Hoop, R. Pieters, E. Siringil, M. S. Sakar, B. J. Nelson, S. Pane, *Mater. Horiz.* 2016, **3**, 113; c) J. Li, V. V. Singh, S. Sattayasamitsathit, J. Orozco, K. Kaufmann, R. Dong, W. Gao, B. Jurado-Sanchez, Y. Fedorak, J. Wang, *ACS Nano* 2014, **8**, 11118.

[23] a) J. Li, T. Li, T. Xu, M. Kiristi, W. Liu, Z. Wu, J. Wang, *Nano Lett.* 2015, **15**, 4814; b) V. Garcia-Gradilla, J. Orozco, S. Sattayasamitsathit, F. Soto, F. Kuralay, A. Pourazary, A. Katzenberg, W. Gao, Y. Shen, J. Wang, *ACS Nano* 2013, **7**, 9232.

[24] Z. Miao, D. Xu, J. Ouyang, G. Guo, X. Zhao, Y. Tang, *Nano Lett.* 2002, **2**, 717.

[25] a) A. Di Paola, G. Cufalo, M. Addamo, M. Bellardita, R. Campostrini, M. Ischia, R. Ceccato, L. Palmisano, *Colloids Surf. A Physicochem. Eng. Asp.* 2008, **317**, 366; b) R. Li, Y. Weng, X. Zhou, X. Wang, Y. Mi, R. Chong, H. Han, C. Li, *Energy Environ. Sci.* 2015, **8**, 2377.

[26] a) B. A. Wols, C. H. M. Hofman-Caris, *Water Res.* 2012, **46**, 2815; b) V. I. Parvulescu, H. Garcia, in *Catalysis.* 2011, **23**, 204.

[27] a) S. Linic, P. Christopher, D. B. Ingram, *Nat. Mater.* 2011, **10**, 911; b) Y. Nakato, K. Ueda, H. Yano, H. Tsubomura, *J. Phys. Chem.* 1988, **92**, 2316.

[28] K. H. Leong, H. Y. Chu, S. Ibrahim, P. Saravanan, *Beilstein J. Nanotechnol.* 2015, **6**, 428.

[29] A. Zielinska-Jurek, *J. Nanomater.* 2014, **2014**, 17.

[30] A. G. Dylla, K. J. Stevenson, *Chem. Commun.* 2011, **47**, 12104.

[31] F. B. Li, X. Z. Li, *Chemosphere* 2002, **48**, 1103.

[32] L. Liu, S. Park, *Chem. Mater.* 2011, **23**, 1456.

[33] S. M. Kim, L. Liu, S. H. Cho, H. Y. Jang, S. Park, *J. Mater. Chem. A* 2013, **1**, 15252.

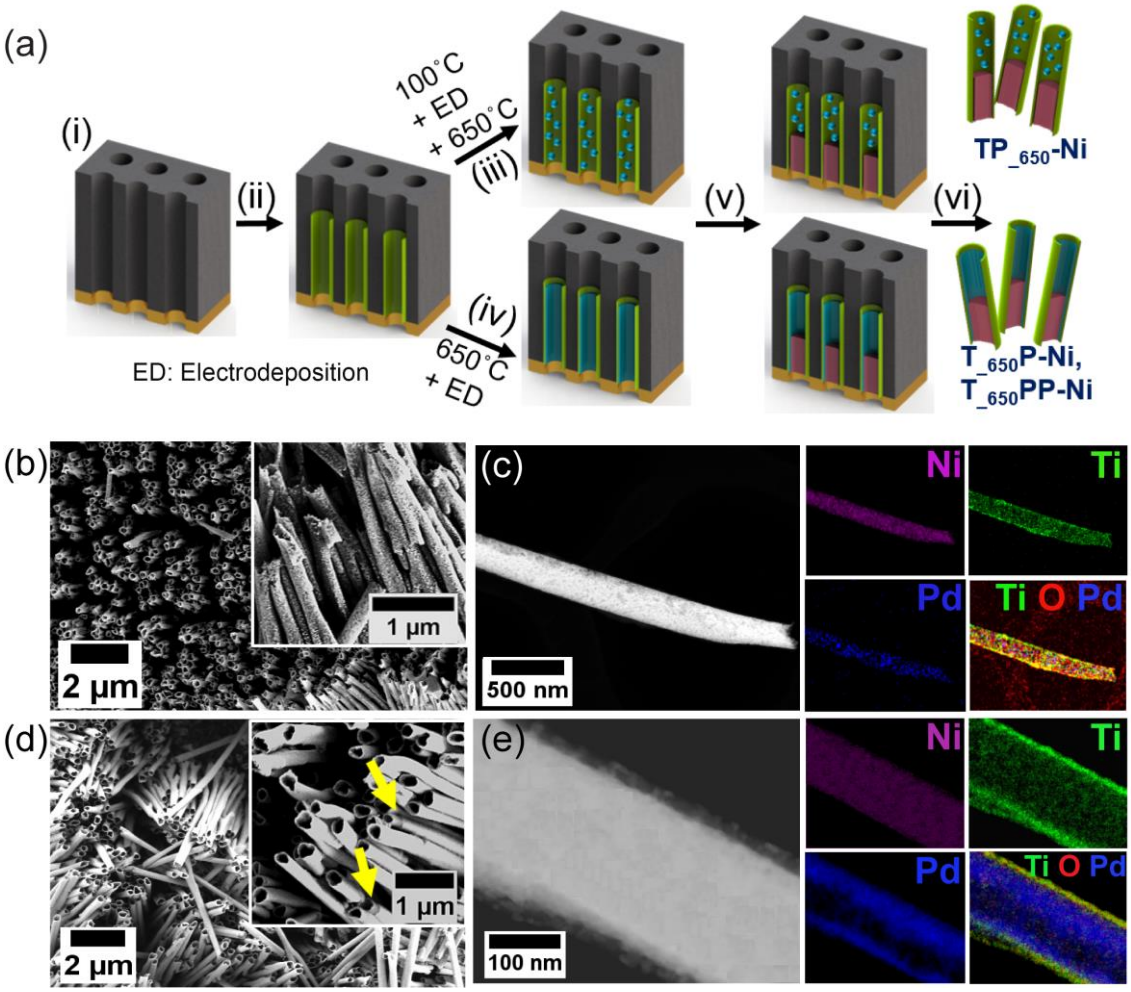

Figure 1. Fabrication overview of hybrid NTs: (a) (i) Au sputtered on one side of AAO templates, (ii) electrochemically induced sol-gel deposition of TiO_2 NTs, (iii) electrodeposition (ED) of Pd NPs inside TiO_2 NTs dried at 100 ˚C, followed by annealing at 650 ˚C, (iv) electrodeposition of Pd NTs inside TiO_2 NTs annealed at 650 ˚C, (v) electrodeposition of Ni NWs, followed by (vi) etching of AAO templates. (b) SEM image showing an overview of freestanding $TP_{\_650}$ NTs and the inset shows its magnified image with presence of NPs distributed on the TiO_2 surface. (c) HAADF STEM image of a single $TP_{\_650}$-Ni NT and its corresponding EDX Maps obtained for Ni, Ti, Pd and a superimposed image that clearly shows the presence of Pd as NPs inside a TiO_2 NT. (d) SEM image showing an overview of freestanding $T_{\_650}P$ NTs and the inset shows its magnified image. (e) HAADF STEM image of a single $T_{\_650}P$-Ni NT and its corresponding EDX maps obtained for Ni, Ti, Pd where the superimposed image clearly shows a coaxial TiO_2-Pd NT structure.

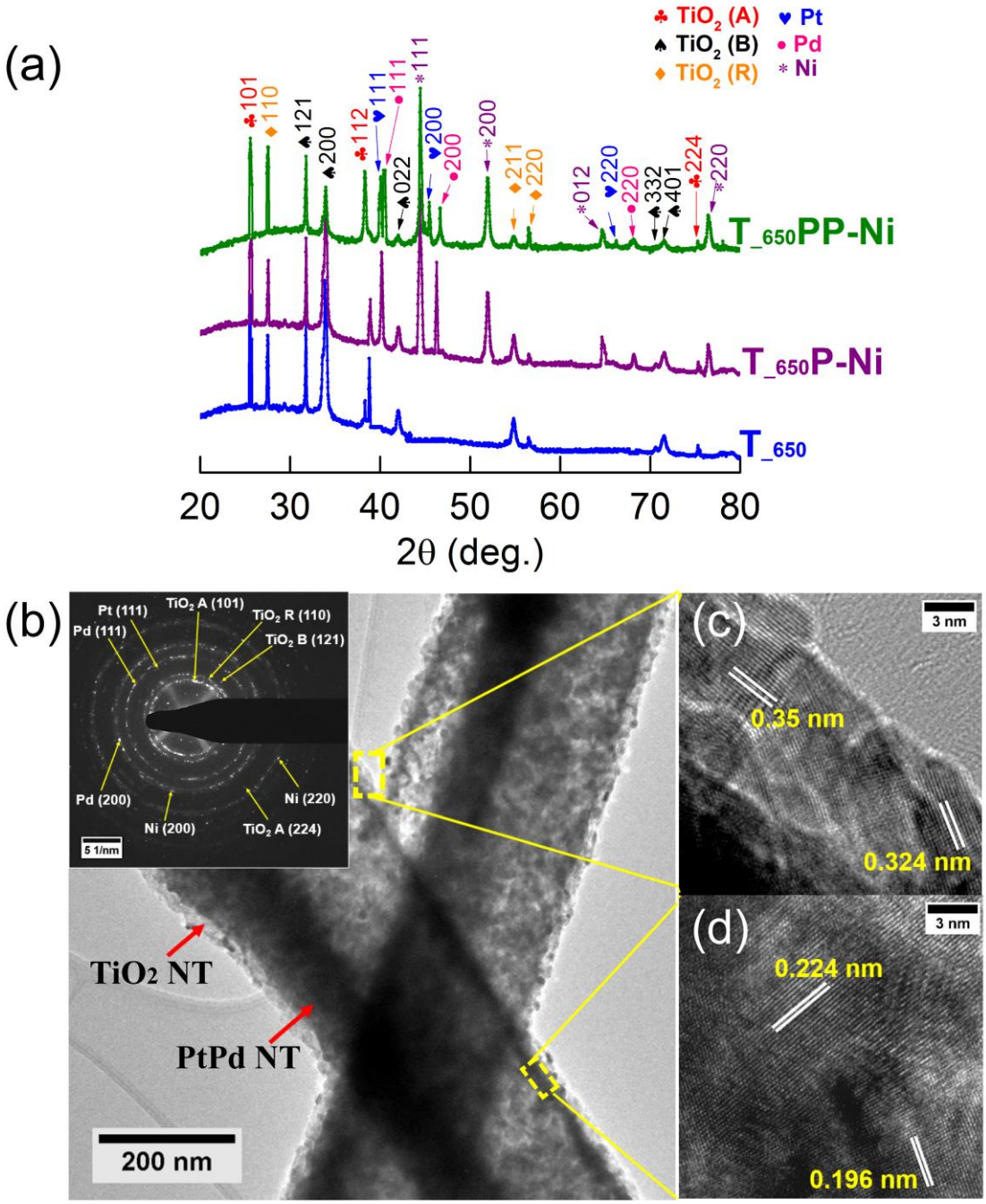

Figure 2. Structural characterisation of hybrid NTs. (a) XRD patterns obtained for hybrid TiO_2 NTs. (b) TEM image showing two overlapping $T_{_650}$PP-Ni NTs. In the inset, its corresponding diffraction pattern can be observed. (c) HRTEM image obtained from the outermost shell showing the presence of anatase and rutile TiO_2 whereas, (d) the HRTEM image obtained from the interface region shows the presence of metallic Pt and Pd.

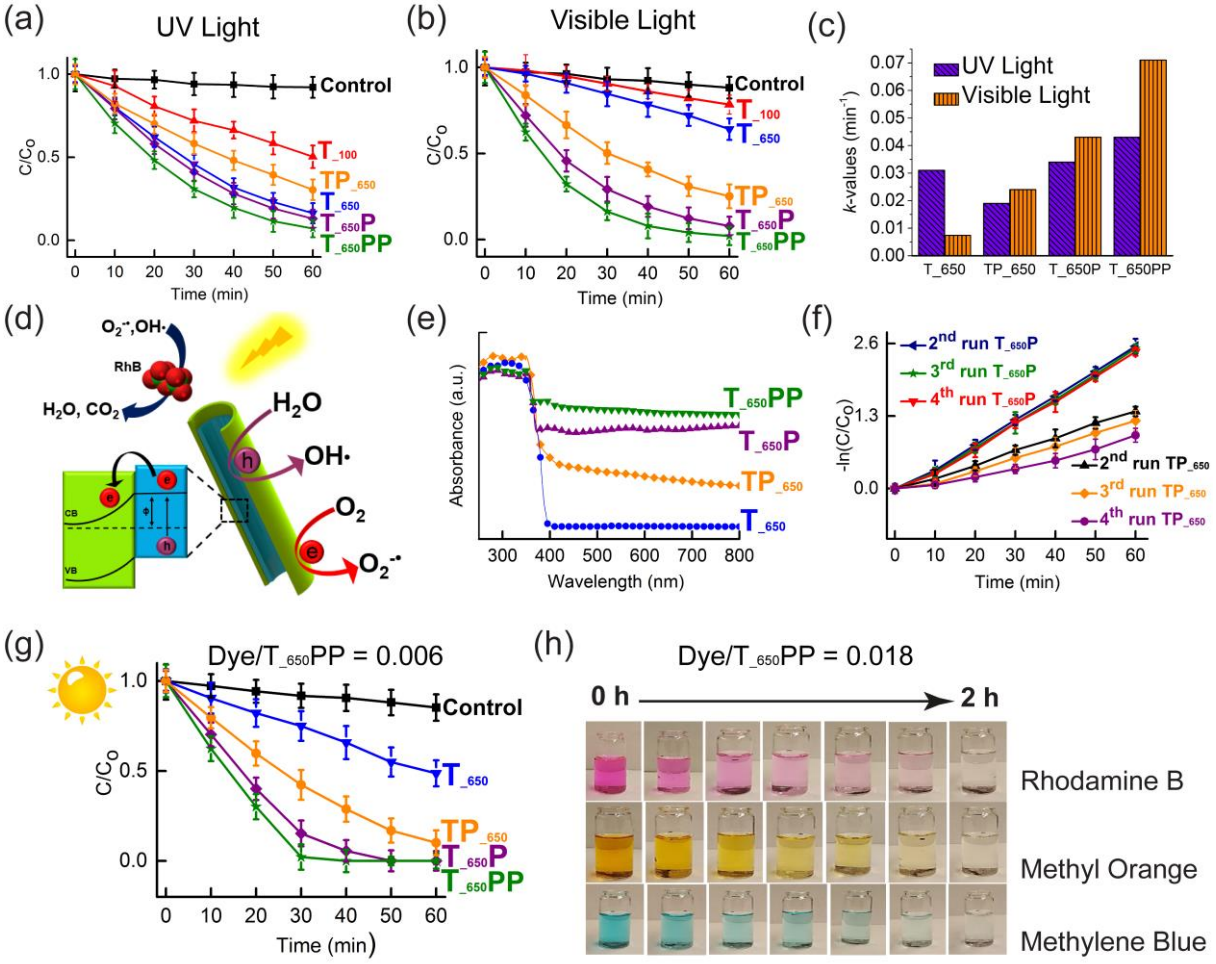

Figure 3. Photocatalytic degradation of RhB dye using hybrid NTs. Photocatalytic degradation curves obtained for RhB under (a) UV light irradiation and (b) visible light irradiation. (c) Comparison of degradation rate constants under UV and visible light for RhB. (d) Photocatalytic degradation scheme of hybrid coaxial NTs under visible light showing the formation of electron-hole pairs and how they degrade organic pollutants. (e) UV-Vis DRS spectra obtained for TiO_2 NTs with and without noble metals. (f) Linear fit log plots of three consecutive degradation curves showing the reusability trend exhibited by $TP_{\_650}$ NTs and $T_{\_650}P$ NTs. (g) Photocatalytic degradation curves obtained under natural sunlight, where RhB concentration was 4 mg L^{-1} and (h) visual color change of three different organic dyes at a higher concentration of 12 mg L^{-1} under natural sunlight over time.

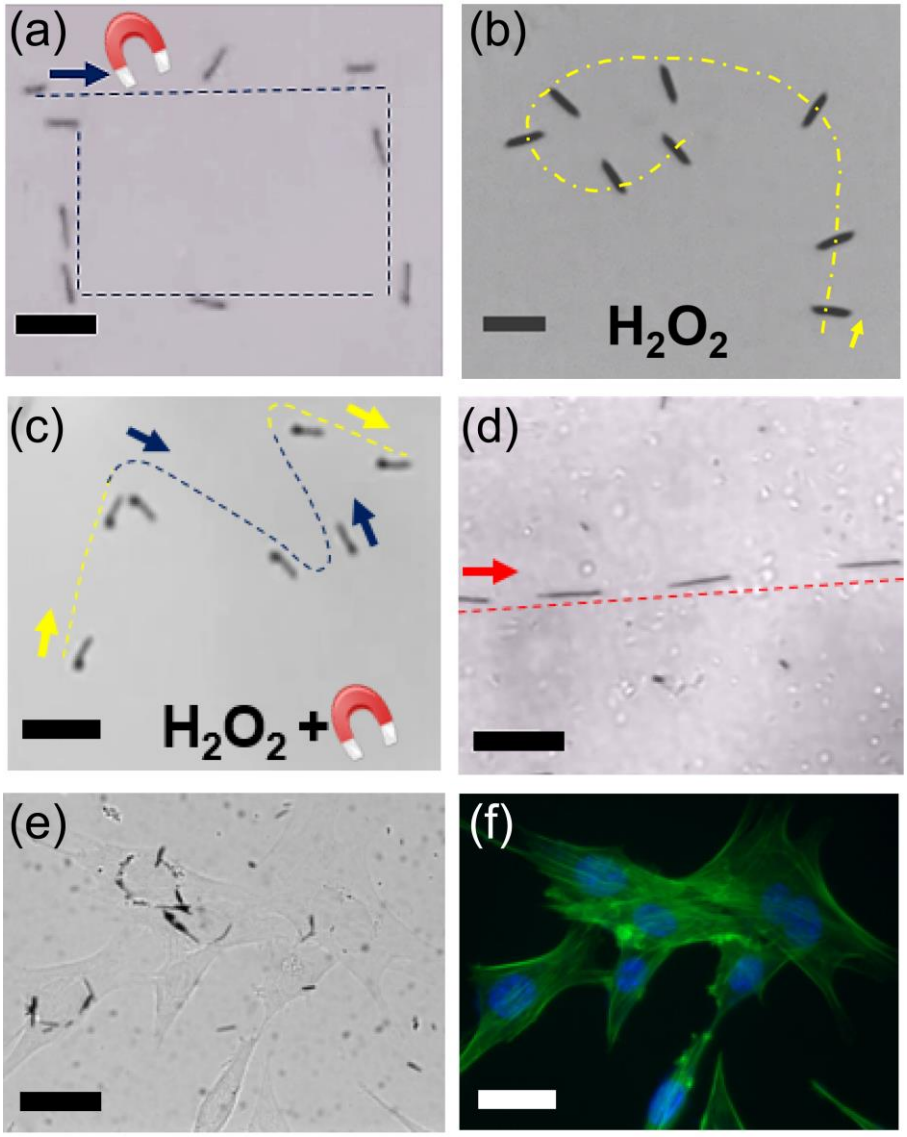

Figure 4. Propulsion mechanisms and biocompatibilty of hybrid TiO_2-PtPd-Ni NTs. (a) Time lapse image showing magnetic manipulation of a hybrid NT along a pre-planned trajectory (blue); (b) Time lapse image showing an autonomous motion demonstrated by a single hybrid NT in 5% H_2O_2 solution (yellow); (c) time lapse image of a hybrid NT showing dual propulsion exhibiting an autonmous motion (yellow) which can also be guided by wireless magnetic fields (blue). (e) Optical image of NIH 3T3 fibroblast cells cultured on TiO_2-PtPd-Ni NTs showing cell proliferation; and (f) its corresponding fluorescence image with stained nucleus (blue) and actin (green) showing healthy cells with extended actin fibers. Scale bars indicate 30 μm (a-c), 40 μm (d), 80 μm (e,f).

Coaxial TiO_2-PtPd-Ni hybrid nanotubes exhibit greatly enhanced visible light photocatalyic activity: a 100% degradation of organic pollutant under visible and natural sunlight with high stability. Combined with multiple locomotion strategies, these highly efficient and cost-effective hybrid photocatalytic nanomachines have the potential to be reused for practical water remediation applications in complex and challenging environments.

Keywords: TiO_2; Visible light photocatalysis; Core-shell nanotubes; Electrochemical synthesis; Micromanipulation

Authors: F. Mushtaq, A. Asani, M. Hoop, Dr. X.-Z. Chen*, Dr. D. Ahmed, Prof. Dr. B. J. Nelson, Dr. S. Pané*

Multi-Scale Robotics Lab (MSRL), Institute of Robotics and Intelligent Systems (IRIS), ETH Zurich, CH-8092 Zurich, Switzerland.

Title: Highly Efficient Coaxial TiO_2-PtPd Tubular Nanomachines for Photocatalytic Water Purification with Multiple Locomotion Strategies

TOC Figure: